Effects of Crystallographic Orientation and Grain Morphology on Crack Tip Stress State and Plasticity

M.E. Kartal[1], M.A. Cuddihy[2,*] and F. P. E. Dunne[2]

[1]Department of Engineering Science, University of Oxford, Parks Road, Oxford OX1 3PJ, UK

[2]Department of Materials, Imperial College London, London SW7 2AZ, UK

Abstract

The Sih, Paris and Irwin analytical solution for cracks in anisotropic elastic media has been developed for an hcp Ti single crystal and shown to lead to crack tip normal stresses which are independent of crystal orientation but other stress components which are dependent. Detailed finite element studies confirm that the stress intensity remains independent of crystal orientation but ceases to do so in an edge-cracked bi-crystal.

The incorporation of crystallographic slip demonstrates that single-crystal crack tip stresses largely remain independent of crystal orientation but that the plastic zone size and shape depends greatly upon it. Significant differences result in both the magnitude and extent of the plasticity at the crack tip with crystallographic orientation which can be quite different to that predicted using Mises plasticity. For an edge crack terminating in a bi-crystal, the slip fields which result depend upon both crystal mis-orientation and morphology.

Keywords: Stress intensity; crystal plasticity; anisotropy; titanium alloys; cold dwell fatigue; crystallographic slip.

* Corresponding author: mitch.cuddihy@imperial.ac.uk

Nomenclature

σ_{ij} = Stress in the direction indicated by the subscript, x-y Cartesian and r-θ for polar

ε_{ij} = Strain in the direction indicated by the subscript, x-y Cartesian and r-θ for polar

$\varphi_{1,2}$ = Euler angle

s_{ij} = Element of the compliance matrix

μ_j = Roots of the characteristic equation, j = 1, 2, 3, 4

K_j = Stress intensity factor, j = I or II depending on mode

$\boldsymbol{R}$ = Rotation matrix

$\boldsymbol{T}$ = Transformation matrix

$\boldsymbol{S}$ = Rotated compliance matrix

a, b = Crack length and plate width, respectively

1. Introduction

Since the 1950s, titanium has been the mainstay for critical rotating components such as discs and blades, in the low to high pressure sections of the compressor of gas turbine engines [1]. Titanium alloys offer several key advantages including reduced density, high fracture toughness, high strength and corrosion resistance. Indeed, the latter two qualities have led to extensive titanium use in biomedical devices [2]. Particular alloys may be used throughout aircraft production, such as landing gear, nacelles and fuselage [3]. The 'workhorse' of the aerospace industry is the alloy Ti-6Al-4V which in some instances may make up 80-90% of the titanium used on an aircraft [3], and accounts for approximately 56% of the market share of all titanium production [2]. Commercially pure (CP) titanium only accounts for 26%, with the remainder largely occupied by various alpha and alpha-beta alloys.

Cold dwell fatigue [1,4-10] refers to a failure mode observed in titanium alloy components due to a stress hold (dwell) at peak stress during cyclic loading at ambient temperatures. This issue, first recognised in the early 1970s after the uncontained failure of two titanium alloy aero-engine fan discs [1], remains a serious concern for all engine manufacturers [4].

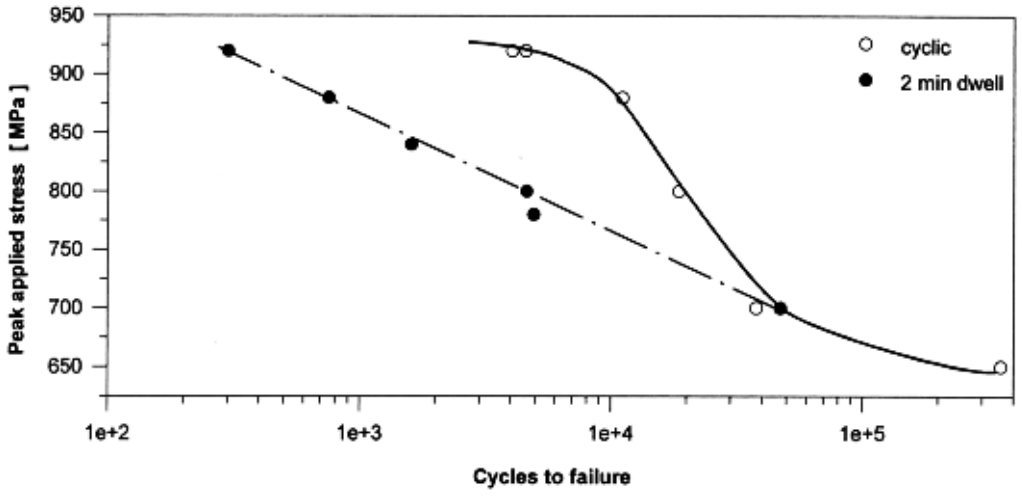

Figure 1 - S-N curves illustrating dwell-debit [5]

Fig. 1 shows the results of a fatigue performance study on disc samples of the titanium alloy IMI834 [5] in which the effect on lifespan of the two minute dwell may be clearly seen. Research efforts have been focused on producing a quantitative predictive relationship between structure, texture and properties, but have not been completely successful. Aero-engine manufacturers such as Rolls-Royce consequently rely on expensive and time

consuming component tests which attempt to establish empirical relations that may be incorporated in the design methodologies [6].

The mechanistic origin of the cold dwell debit is argued to be fatigue facets which are micro cracks occurring in areas of near-uniform crystallographic orientation in titanium alloys [12] and have been observed in experiment many times [5], [11]–[13]. Fig. 2, taken from an experiment conducted by Sinha et al. [13], shows a facet fracture surface on a sample of Ti-6242 (or Ti-6Al-2Sn-4Zr-2Mo). This dwell-fatigue test included a load control of a peak stress of 869 MPa and included a dwell of two minutes at this peak stress. The dwell fatigue specimen failed in 447 cycles whereas the normal, cyclically loaded, fatigue specimen failed after 24,000 cycles; a dwell-debit of 54. These two specimens had the same specimen geometry and were machined from the same forging. It is noted by Sinha et al [13] that while the precise values for lifespan reduction (dwell-debit) vary, they are consistently large.

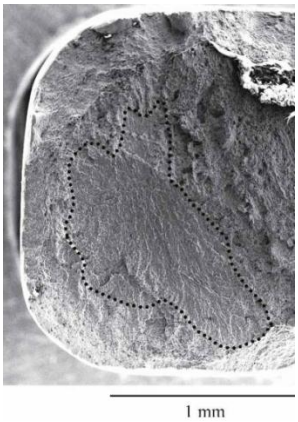

Figure 2 - Dwell-fatigue fracture surface, faceted initiation site marked by a dashed line, after [13]

Cold dwell facets are thought to develop progressively (as opposed to instantaneously) but nonetheless very much more rapidly than under conventional fatigue regimes. Once nucleated, in a region usually characterised by uniform basal crystallographic orientation, they are sometimes found to remain unchanged during subsequent cyclic loading, but other times to propagate into adjacent grains.

Early pioneering work by Rice et al. in the 1980s [14-17] developed and applied asymptotic analyses to solve for crack tip fields in elastic-ideally plastic fcc and bcc single crystals; this approach was extended to hcp and layered materials by Gupta [18]. Cuitino and Ortiz [19] investigated three dimensional crack tip fields in single crystal copper specimens under four-point bending test conditions; their numerical results agreed with that of the earlier analytical

studies of Rice et al. The present work builds upon the analytical HRR-fields based research of Rice et al by utilising the full computational power of crystal plasticity finite element methods.

The first to address crack nucleation in a rigorous manner was Stroh [20]. Later studies have addressed facet nucleation criteria (e.g. Kirane and Ghosh [21], and Dunne and Rugg [22]) in particular, hypothesised the role of normal and shear stress relative to a basal plane in nucleation. However, the mechanics of nucleated facets, either partially developed across a region of uniform crystallographic orientation, or subsequently propagating into adjacent grains, has not received attention. Particularly, the stresses and stress intensities and localised (plastic) slip at the crack tip generated by a facet, and influenced by local crystallographic details of morphology and orientation, leading to very strong elastic and plastic anisotropy, have not been addressed.

This paper therefore presents a fundamental assessment of stress and stress intensity generated by an existing facet within, initially, a single crystal in which the crystallographic orientation is varied with respect to remote loading direction. The work is extended to consider the presence of a facet within bi-crystals with specified and varied crystallographic orientations and sizes in order to investigate the roles of grain constraint and crystallographic orientation in stress and stress intensity local to the crack tip. Finally, the anisotropic nature of the slip developed local to the facet tip is investigated with respect to crystallographic orientation.

In the next section, the fundamental analysis of stress intensities in anisotropic media are addressed, which are specialised for hexagonal close packed (hcp) elastic anisotropy. An analytical analysis is presented of the stresses local to an edge crack in an elastically anisotropic hcp single crystal and their dependence on crystallographic orientation is investigated. An edge crack in an elastically anisotropic Ti hcp bi-crystal is then addressed using a finite element model in order to investigate the role of the combination of crystallographic orientation on stress and stress intensity at the crack tip. This is followed by a brief description of the crystal plasticity slip model which is employed to investigate the accumulated slip fields ahead of the crack tip, taking full account of the anisotropic nature of the slip activity. We then address the nature of the crystal slip fields established at the crack tip, and their dependence on crystallographic orientation and relative grain size. In passing,

the slip fields so determined are compared with the plastic strain fields obtained from Mises plasticity, but while maintaining the elastic anisotropy of the crystals. Finally, a quantitative analysis of accumulated slip at the crack tip as a function of crystallographic orientation is also presented.

2. Analytical Crack-tip Stress Fields in 2D Anisotropic Media

In this section, elastic anisotropy associated with hcp crystal structure is considered since this is of importance in the context of Ti alloy facet nucleation. An edge crack is first considered in a homogeneous single crystal with arbitrary crystallographic orientation with respect to the crack direction and remote loading.

2.1 Stress Field Formulation

Consider a plate, with its major dimensions lying in the *xy* plane and the *z*-axis directed into the page, as shown in Fig. 3(a). The *x* and *y* axes are parallel and normal to the crack surface respectively.

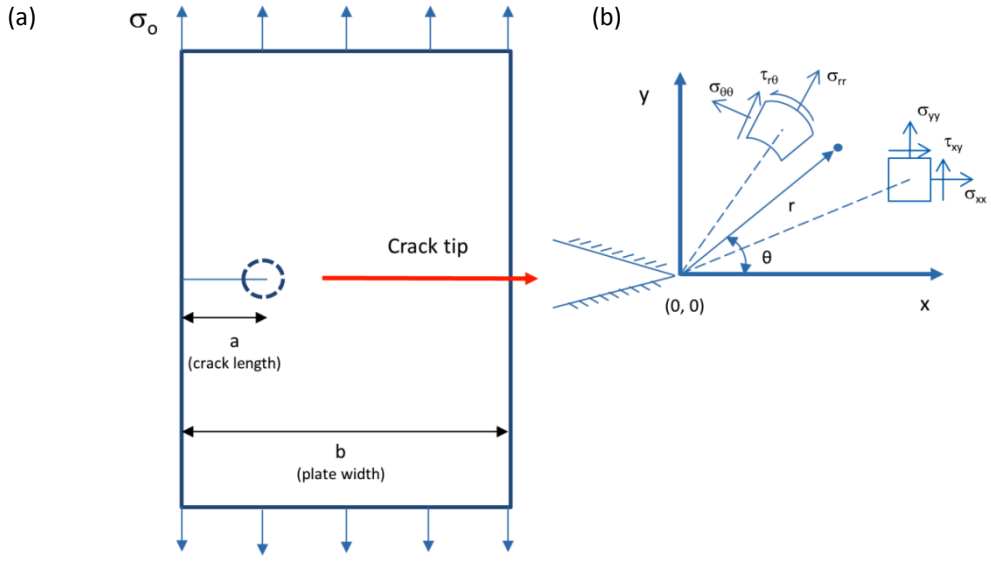

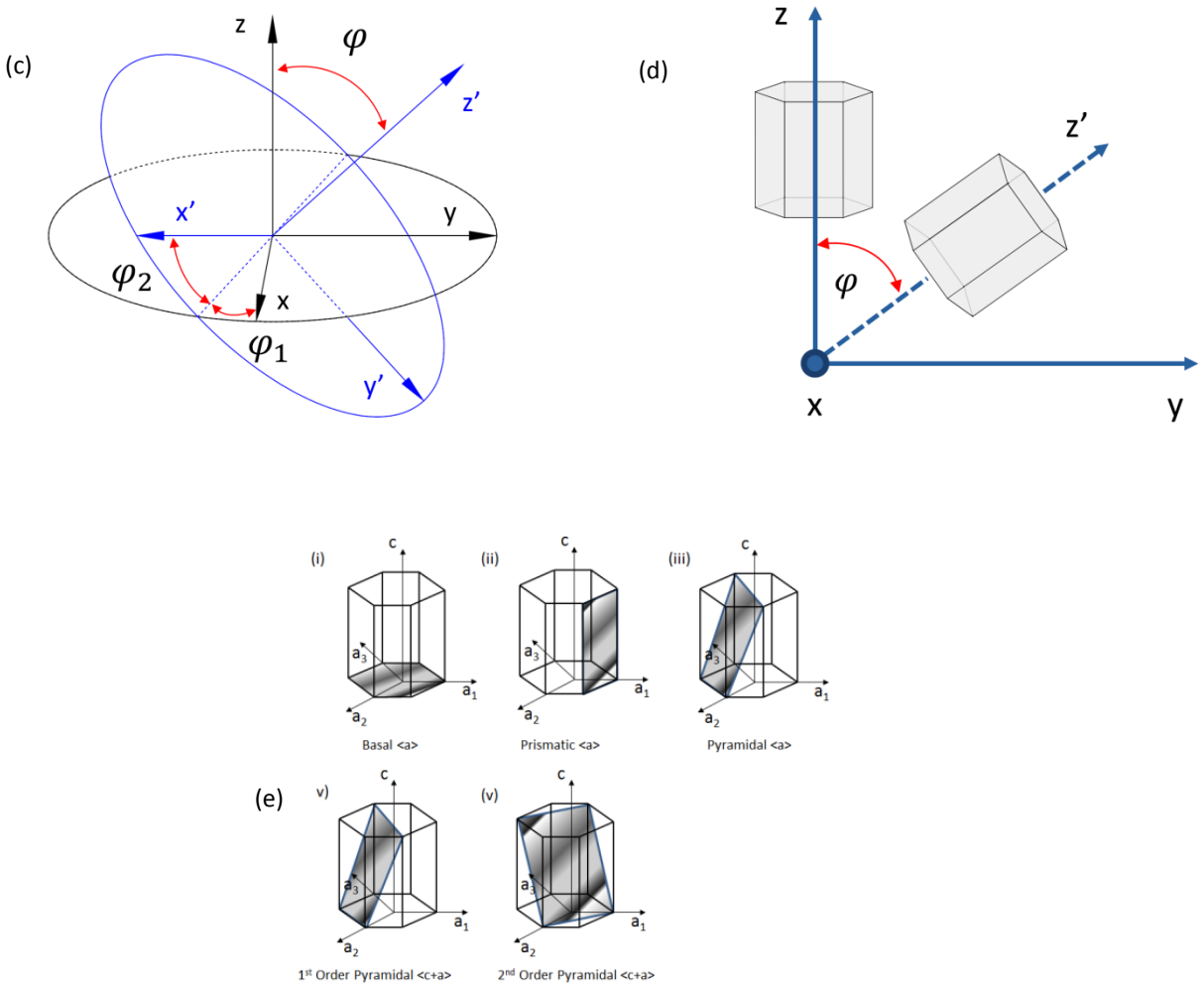

Figure 3 - (a) General description of an edge crack in a half-plane, (b) elemental stresses in polar and Cartesian coordinates, (c) Euler angles, (d) crystal rotation and (e) the hcp crystal anisotropic slip systems

Assuming plane stress (i.e. $\sigma_z = 0$), the solution is formed from an Airy stress function $U(x, y)$ which satisfies the equations of equilibrium and as such the stresses are defined as:

$$\sigma_x = \frac{\partial^2 U}{\partial y^2} \quad , \quad \sigma_y = \frac{\partial^2 U}{\partial x^2} \quad , \quad \sigma_{xy} = -\frac{\partial^2 U}{\partial x \, \partial y} \tag{1}$$

For the *xy* plane, the compatibility equation takes the form:

$$\frac{\partial^2 \varepsilon_x}{\partial y^2} + \frac{\partial^2 \varepsilon_y}{\partial x^2} = \frac{\partial^2 \gamma_{xy}}{\partial x \, \partial y} \tag{2}$$

Combining the compatibility and equilibrium equations using anisotropic Hooke's Law, we obtain the governing differential equation for the anisotropic theory of elasticity

$$s_{22}\frac{\partial^4 U}{\partial x^4} - 2s_{26}\frac{\partial^4 U}{\partial x^3 \partial y} + (2s_{26} + s_{55})\frac{\partial^4 U}{\partial x^2 \partial y^2} - 2s_{16}\frac{\partial^4 U}{\partial x\, \partial y^3} + s_{11}\frac{\partial^4 U}{\partial y^4} = 0 \quad (3)$$

where, s_{ij} are the components of the stress-strain compliance matrix for an anisotropic material (a similar equation may be obtained for plane strain). The 4th order differential equation may be solved by means of a characteristic equation which is:

$$s_{11}\mu_j^4 - 2s_{16}\mu_j^3 + (2s_{12} + s_{55})\mu_j^2 - 2s_{26}\mu_j + s_{22} = 0 \quad (4)$$

noting that μ_j are the roots of this equation and represent the material properties in the stress field equations. Lekhnitskii [23] has shown that the roots of Eq.4 are complex conjugate pairs of the form:

$$\mu_1 = \alpha_1 + i\beta_1, \quad \mu_2 = \alpha_2 + i\beta_2, \quad \mu_3 = \overline{\mu}_1, \quad \mu_4 = \overline{\mu}_2 \quad (5)$$

Further details of the derivation are available in Liebowitz [24], but the pertinent equations for Mode I are:

$$\sigma_{xx} = \frac{K_I}{\sqrt{2r}} Re\left[\frac{\mu_1\mu_2}{\mu_1 - \mu_2}\left(\frac{\mu_2}{\sqrt{(cos\theta + \mu_2 sin\theta)}} - \frac{\mu_1}{\sqrt{(cos\theta + \mu_1 sin\theta)}}\right)\right] \quad (6)$$

$$\sigma_{yy} = \frac{K_I}{\sqrt{2r}} Re\left[\frac{1}{\mu_1 - \mu_2}\left(\frac{\mu_1}{\sqrt{(cos\theta + \mu_2 sin\theta)}} - \frac{\mu_2}{\sqrt{(cos\theta + \mu_1 sin\theta)}}\right)\right] \quad (7)$$

$$\sigma_{xy} = \frac{K_I}{\sqrt{2r}} Re\left[\frac{\mu_1\mu_2}{\mu_1 - \mu_2}\left(\frac{1}{\sqrt{(cos\theta + \mu_2 sin\theta)}} - \frac{1}{\sqrt{(cos\theta + \mu_1 sin\theta)}}\right)\right] \quad (8)$$

The proceeding investigation utilises polar coordinates, see Fig. 3(b); this transformation involves using the following equations:

$$\sigma_{rr} = \sigma_{xx}cos^2\theta + \sigma_{xx}sin^2\theta + \sigma_{xy}sin2\theta \quad (9)$$

$$\sigma_{\theta\theta} = \sigma_{xx}cos^2\theta + \sigma_{xx}sin^2\theta - \sigma_{xy}sin2\theta \quad (10)$$

$$\sigma_{r\theta} = (\sigma_{yy} - \sigma_{xx})sin\theta cos\theta + \sigma_{xy}cos2\theta \quad (11)$$

This is the first study to apply the original Sih et al. [25] derived equations to the particular case of a transversely isotropic material; Lempidaki et al. [26] investigated cubic materials. In this paper we assess the effects of rotating the hcp crystal in 3D space on the crack-tip stress state and investigate the effects of crystallographic orientation.

Any rotation of a crystal in three-dimensional Euclidean space may be obtained by patterns of successive rotations; indeed there are many possible approaches, such as Rodriguez parameters or quaternions, but the approach used in this study follows the Bunge convention, common in materials science [27]. This approach considers three rotations about the Z-X-Z' axes, where Z' is the new local Z-axis (refer to Fig. 3(c)). The product of these individual rotations gives the overall rotation matrix $\boldsymbol{R}$ given by

$$\boldsymbol{R} = \boldsymbol{R}_{\varphi_1}\boldsymbol{R}_{\varphi}\boldsymbol{R}_{\varphi_2} \tag{12}$$

Consider the rotation of the stress tensor

$$\boldsymbol{\sigma}' = \boldsymbol{R}\ \boldsymbol{\sigma}\ \boldsymbol{R}^T \tag{13}$$

Converting the stress tensors to vector form yields:

$$\underline{\sigma}' = \boldsymbol{T}\,\underline{\sigma} \tag{14}$$

The $\boldsymbol{T}$ matrix now contains the details of the rotation applied to the stress vector so that the compliance matrix, for example, is rotated using the following relation:

$$\boldsymbol{S}_{3D\ Rot} = \boldsymbol{T}^{-1}\boldsymbol{S}\,\boldsymbol{T} \tag{15}$$

The above procedure now allows the calculation of the compliance matrix for any specified crystallographic rotation - further details of the rotation are provided in Appendix A.

It has been demonstrated by Sih et al. [25] that the stress intensity factors for isotropic and anisotropic materials are identical under conditions of self-equilibrating loads. Therefore, if the stress intensity factor is already known for a problem involving an isotropic medium, then it may be applied to that of an anisotropic one. This is contrary to the results of Bao et al. [28], in which it is shown that independence is lost, but this is due to notch geometry. For the case of an infinitesimal crack, as Sih et al have shown, the stress intensity remains independent of the elastic properties, be they anisotropic or isotropic.

As the above equations (6-8) describe the general stress state near a crack tip for a central crack in an infinite medium [25], appropriate selection of stress intensity factor is necessary to apply them the case of an edge crack. In this study the function for K_I used is that which was developed by Brown and Srawley [29]:

$$K_I = \sigma_0\sqrt{\pi a}\left(1.12 - 0.23\left({}^{a}/_{b}\right) + 10.6\left({}^{a}/_{b}\right)^2 - 21.7\left({}^{a}/_{b}\right)^3 + 30.4\left({}^{a}/_{b}\right)^4\right) \tag{16}$$

2.2 Stresses at Crack Tip in hcp Single Crystal Titanium

The elastic anisotropic stress field theory allows for the calculation of the stress components local to the crack tip in a single hcp crystal subject to remote uniaxial loading. The crystal is 200 x 200μm in size, with an edge crack of length 10 μm, under a 100MPa tensile load, as depicted in Fig. 3(a). The crystallographic orientation is specified as shown schematically in Fig. 3(d). The anisotropic elastic properties used for a representative titanium alloy are given in Appendix B; these properties are specified in the reference configuration. The rotation scheme described in the previous section is used to generate the correct rotated s_{ij} values for the characteristic equation (Eq. 4). Upon solving this quartic equation, the required μ_j material parameters may be inserted into the stress field equations. Using this methodology, the y-direction stress components were calculated for differing crystallographic orientations (i.e. φ = 0°, 45°, 60°, 90°) along a line θ = 0, and are given in Fig. 4. For clarity, we focus predominantly on one axis of rotation in order to show the variation due to rotation in detail. The angular ranges are chosen to capture the shift of <a> type deformation to <c+a> type, i.e., considering the c-axis parallel to the z-axis in the first instance and parallel to the y-axis in the second. However, an arbitrary rotation (φ_1 = 30°, φ = 45°, φ_2 = 55°) is included for completeness.

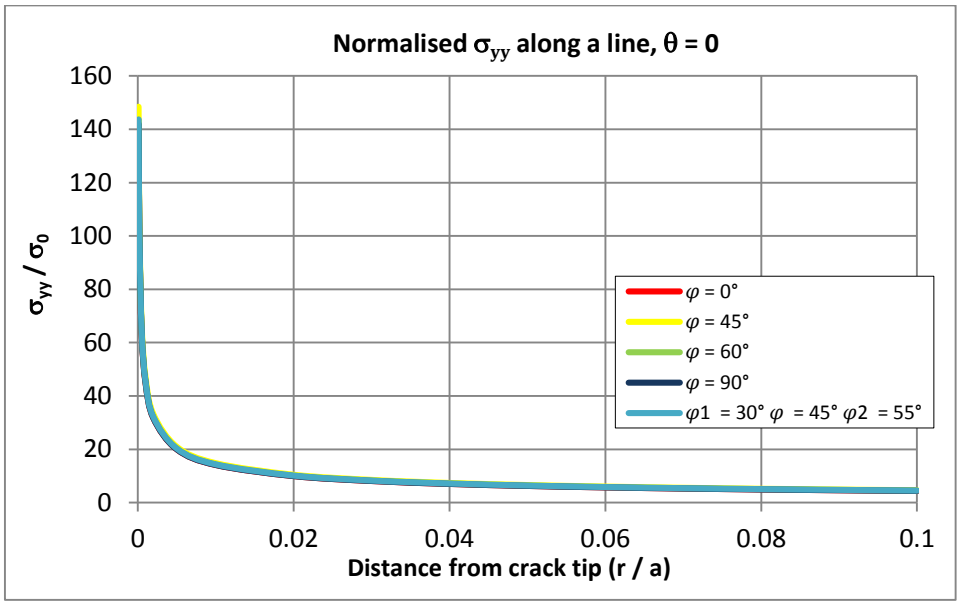

Figure 4 - Stress ahead of the crack tip along the line θ= 0, refer to Fig. 3(b)

It is clear that changes in the orientation have no effect on this component of stress. However, due to the fact that stress is an inverse function of the square root of the distance from the

crack tip it was felt that calculations in polar co-ordinates would give a better description of the stress state. As before, a varied series of crystallographic orientations (i.e. φ = 0°, 30°, 45°, 60°, 90°) were considered and polar stresses at a specified distance from (r = 0.5μm) and in a full circle around the crack tip were calculated (Eq. 9-11). The distance of 0.5 μm was selected so as to be fully representative of the K-field. In Fig. 5(a)-(c), the polar components of stress are shown against the circumferential distance around the crack tip. The radial stresses in Fig. 5(a) show the biggest variation in magnitude for varying crystallographic orientation, but remain modest; this is echoed by the shear stresses. The hoop stresses are independent of crystallographic orientation.

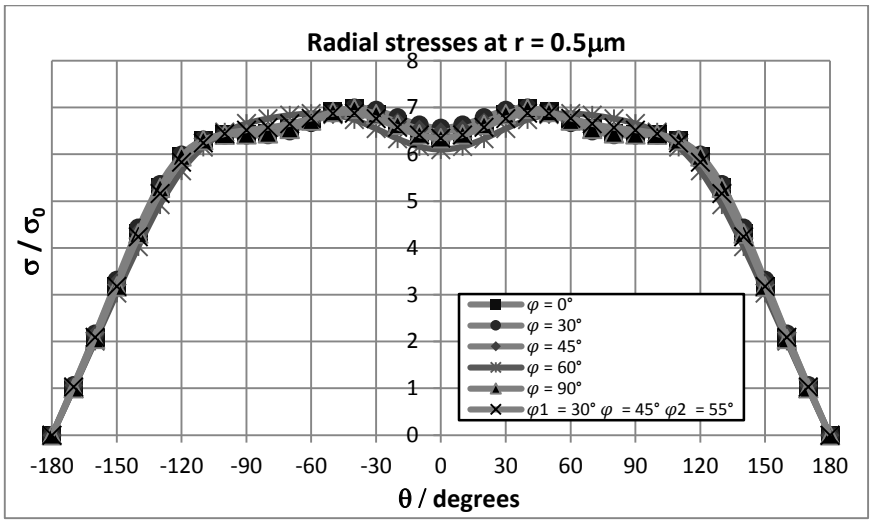

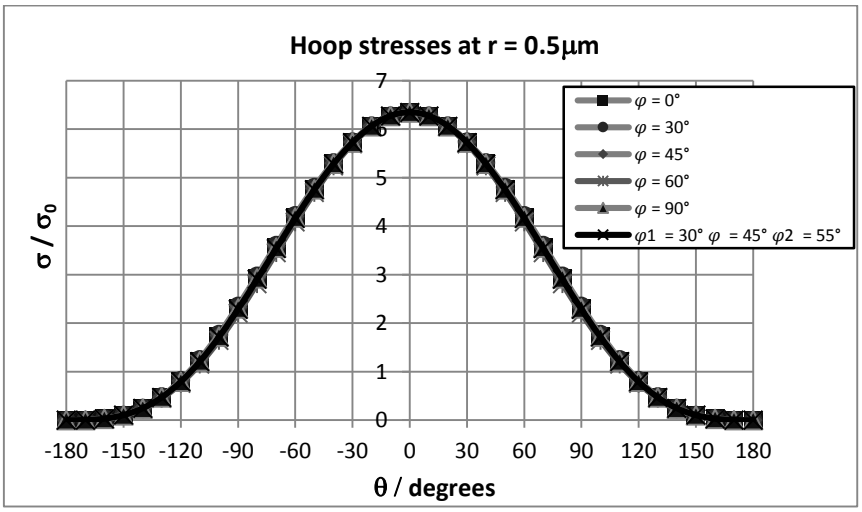

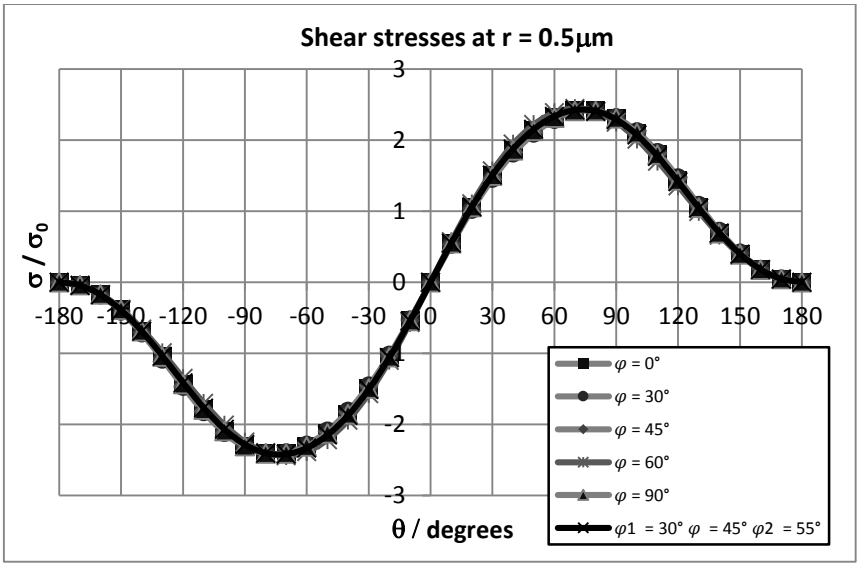

Figure 5 - Normalised radial (σ_{rr}/σ_0), circumferential ($\sigma_{\theta\theta}/\sigma_0$) and shear ($\sigma_{r\theta}/\sigma_0$) stress components at a fixed distance from the crack tip, r=0.5 µm

Considered in parallel were the stress intensity factors for the elastic single crystal. These were assessed by means of a finite element model, shown in Fig. 6. The hcp crystal orientation was specified as in the above analytical study. The stress intensity factor was calculated using the *J*-integral approach developed by Rice [30], which has been incorporated within the ABAQUS finite element software. In ABAQUS, a ring of elements is used to calculate the SIF, using the J-integral method. Twenty contours were considered to ensure that the value calculated was stable and consistent.

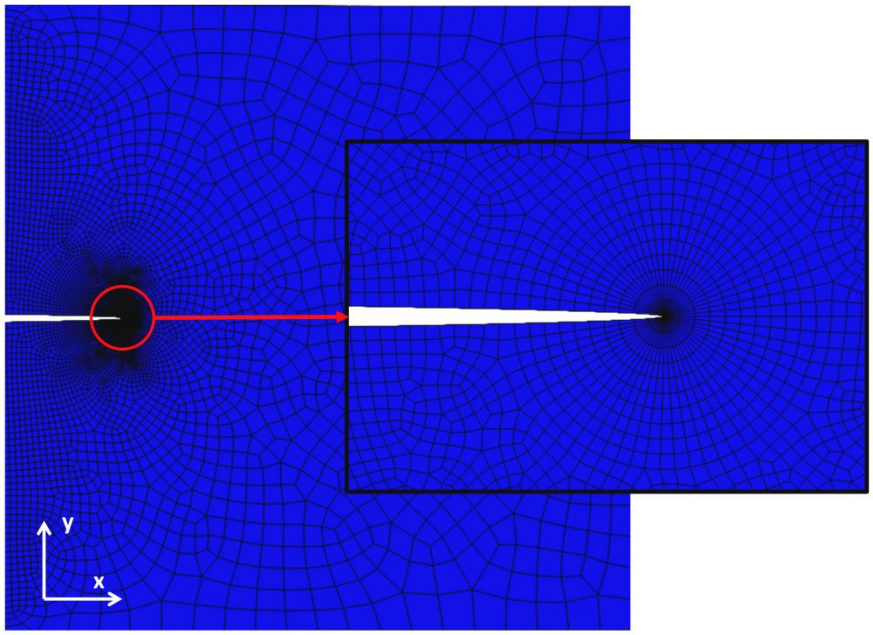

Figure 6 - The finite element discretisation in the region of the crack

Using this method, the stress intensity factors for three particular crystallographic orientations (φ=0°, 60°, 90°) have been calculated and compared with that of a single crystal isotropic elastic plate (which agrees with the Brown and Srawley solution [29]) over various crack length to plate width aspect ratios (*a/b*). Results are shown in Fig. 7, and no variation is apparent for the differing aspect ratios.

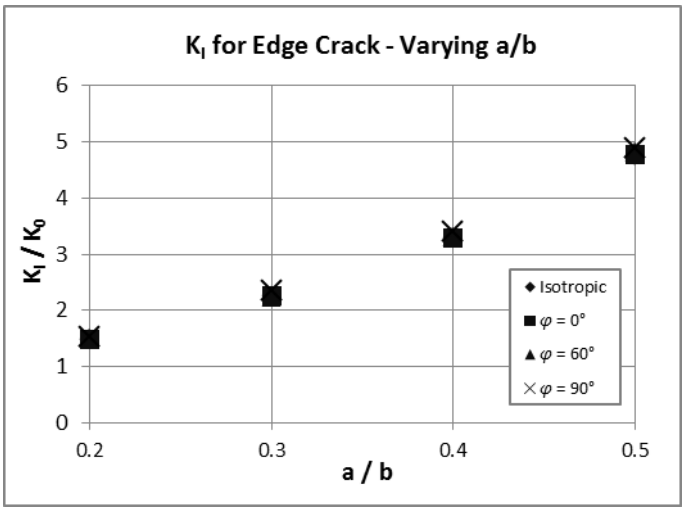

Figure 7 - Variations of the stress intensity factor K_I versus crack length/plate width (*a/b*).

The second case is that of an angled central crack, shown in Fig. 8, in which the crack is orientated at an angle β to the applied tensile stress direction. The angled crack is defined such that the Mode I crack opening is orientated perpendicularly to the crack, and the Mode II sliding is parallel to the crack.

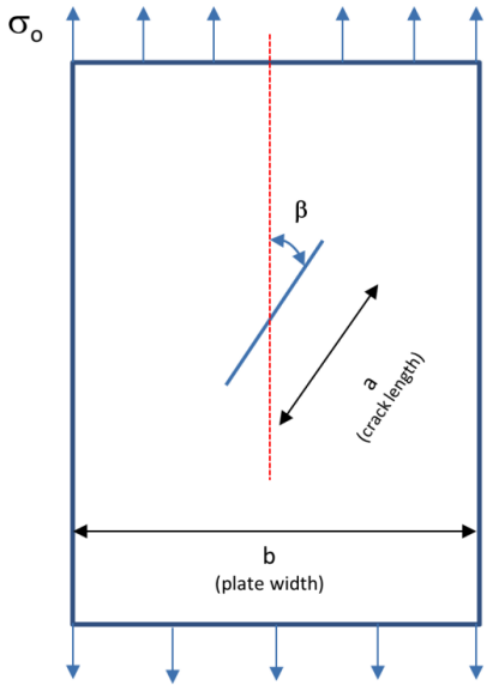

Figure 8 - Angled crack in a plate held in tension

Comparisons of stress intensity results for the isotropic and hcp anisotropic models for the crystallographic orientations are shown in Table 1, for two different planar crack orientations.

Angled Crack (β = 22.5°)	**K_I / K_0**	**K_{II} / K_0**
Isotropic	0.322	0.627
φ = 0°	0.356	0.632
φ = 60°	0.341	0.632
φ = 90°	0.315	0.622

Angled Crack (β = 67.5°)	**K_I / K_0**	**K_{II} / K_0**
Isotropic	1.616	0.615
φ = 0°	1.638	0.608
φ = 60°	1.631	0.609
φ = 90°	1.612	0.624

Table 1: Stress intensity factors for angle cracks

As with the edge crack model, the computational results confirm that the stress intensity factor is indeed independent of the crystallographic orientation, first demonstrated theoretically by Sih et al [19]. In both case, horizontal and angled crack, the results presented are normalized as:

$$\widetilde{K}_i = \frac{K_i}{\sigma_0\sqrt{\pi a}} = \frac{K_i}{K_0}, \qquad 17$$

where $i = I, II$ indicates intensity mode, σ_0 is the remote applied stress and a the crack length for an edge crack or half crack length for a centre crack.

Hence, in the context of edge- and centre-cracked elastically anisotropic hcp single crystal, the stress intensity is independent of crystallography. However, it is anticipated that for a facet crack contained within the bulk of a polycrystal, and terminating within a single grain, that the surrounding grains and their crystallographic orientations likely play a role in the stresses local to the crack tip and in the stress intensity. This is investigated in §2.3 with a finite element bi-crystal model shown schematically in Fig. 9.

2.3 Stress Intensity Factors in a hcp Bicrystal

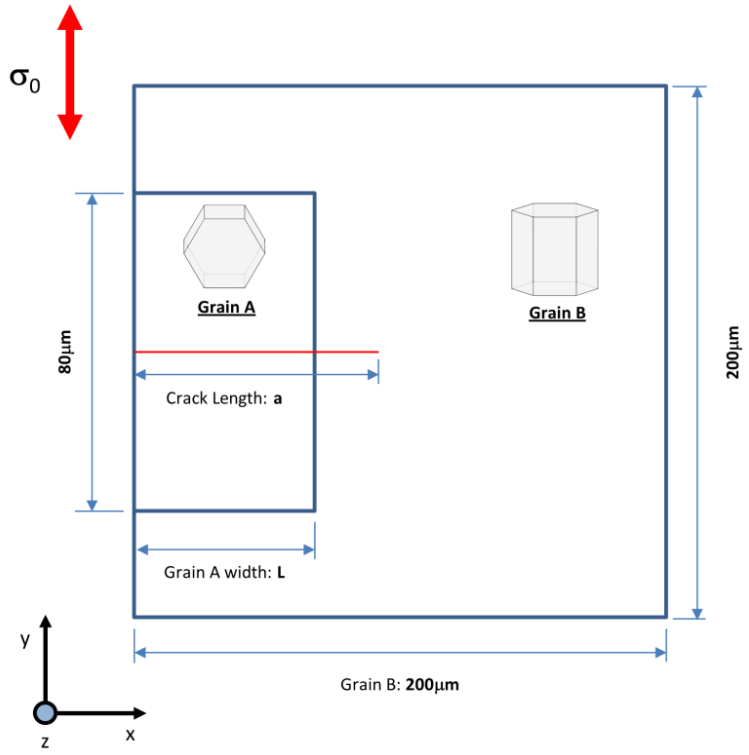

Figure 9 - Schematic diagram of an edge crack in a bi-crystal with dimensions shown and a possible combination of crystal orientations

An edge crack is again considered, but this time traversing grain A, and terminating within grain B shown in Fig. 9. Note that for the purposes of stress intensity factor calculation, the mesh is very fine local to the tip so the contours that were used for the J-integral calculation do not traverse the grain boundary. Example hcp crystallographic orientations for the two grains are shown in the figure. The stress intensity is calculated for the case such that grain B is fixed in two orientations and grain A is progressively rotated about the x-axis from its reference configuration (c-axis parallel to the z-direction) through to 90^o (resulting in its c-axis parallel to the y-axis), as shown in Fig. 3(c). The results of the calculations are shown in Fig. 10(a) where some changes can be seen to the stress intensities resulting from neighbouring grain orientations. Different stress intensities exist for the two initial and differing crystallographic orientations.

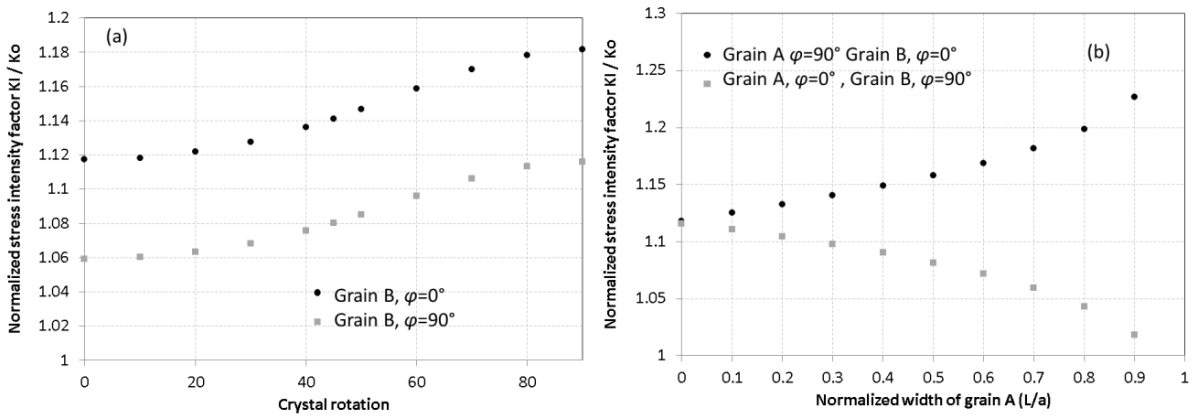

Figure 10 - Effect of the crystallographic orientation on the stress intensity factor for bi-crystal model for (a) the crystallographic orientation of grain *A* with 8 µm width while grain *B* has fixed orientation, and (b) the width of grain *A* when both grains have fixed orientations

The size of grain A relative to B (Fig. 9) is investigated next for two differing crystallographic orientation combinations. The resulting stress intensities are shown in Fig. 10(b). The variations are more substantial here showing the strong dependence of stress intensity on local features of grain morphology. This is potentially important in the context of facet fatigue crack growth (and to a lesser extent nucleation) in Ti alloys. Indeed, Kirane and Ghosh [21] presented a stress-based criterion for facet nucleation which is mixed-mode in nature, reflecting the contributions of both mode I and II, but these stresses and the corresponding stress intensities (for microstructurally short crack growth) are needed at the microstructural level (e.g. within a specific grain). Hence, the analyses above showing the dependency of the stress intensities on local microstructural features such as grain morphology and crystallographic orientation confirm that accurate stresses and corresponding intensities can only be obtained by taking due account of key local microstructural features.
Facet fatigue nucleation is known to be a progressive process taking place over a number of cycles as the crack which has nucleated at a hard grain – soft grain interface propagates through the hard-orientated grain. Hence, the driving stress intensity is likely to be mixed mode and dependent on the local morphology and crystallographic orientations, as shown above.

So far, the analyses carried out have allowed for anisotropic elastic behaviour. We next wish to investigate the crack tip stresses, and the effects of crystallographic orientation, when

crystallographic slip also is allowed to develop at the crack tip, and for this reason, a brief overview of the crystal plasticity model adopted is given in the next section.

3.0 Crystal Plasticity Model

Full details of the crystal plasticity model incorporating strain-gradient plasticity can be found in Dunne et al [10]. The crystal plasticity framework used in this study is based on the multiplicative kinematic decomposition of the deformation gradient into elastic ($\boldsymbol{F}^e$) and plastic ($\boldsymbol{F}^P$) tensors such that

$$\boldsymbol{F} = \frac{\partial \boldsymbol{x}}{\partial \boldsymbol{X}} = \boldsymbol{F}^e \boldsymbol{F}^p \tag{18}$$

Assuming crystallographic slip accounts for deformation, and for now considering just single slip,

$$\boldsymbol{F}^p = \boldsymbol{I} + \gamma\left(\boldsymbol{s} \otimes \boldsymbol{n}\right) \tag{19}$$

in which $\boldsymbol{s}$ and $\boldsymbol{n}$ are slip direction and plane normal respectively, and γ is the magnitude of the slip. Since the material properties at a point are time dependent, it is convenient to write the plastic deformation gradient in rate form as

$$\dot{\boldsymbol{F}}^p = \dot{\gamma}\left(\boldsymbol{s} \otimes \boldsymbol{n}\right) \tag{20}$$

For a spatially varying velocity field, the velocity gradient is defined and decomposed into the symmetric and anti-symmetric parts as

$$\boldsymbol{L} = \dot{\boldsymbol{F}}(\boldsymbol{F}\,)^{-1} = sym(\boldsymbol{L}) + asym(\boldsymbol{L}) \tag{21}$$

The plastic part of the velocity gradient takes the form

$$\boldsymbol{L}^p = \sum_{i=1}^{n} \dot{\gamma}^i \boldsymbol{s}^i \otimes \boldsymbol{n}^i \tag{22}$$

which consists of contributions from all active slip systems, with normal vectors $\boldsymbol{n}^i$ and slip direction vectors $\boldsymbol{s}^i$ corresponding to the i^{th} slip system, and is computed according to a defined slip rule. The flow rule used to describe the slip rate on a slip system is given by

$$\dot{\gamma}^i = \rho_s^m b^{i^2} v exp\left(-\frac{\Delta F}{kT}\right) \sinh\left(\frac{\left(\tau^i - \tau_c^i\right)\gamma_0 \Delta V^i}{kT}\right) \tag{23}$$

with

$$\Delta V^i = l b^{i^2} \text{ where } l = \frac{1}{\sqrt{\psi \rho_s^s}} \tag{24}$$

in which ρ_s^m and ρ_s^s are the mobile and sessile statistically-stored dislocation (SSD) densities, b^i the Burger's vector magnitude for slip system i, ν the frequency of attempts (successful or otherwise) by dislocations to jump the energy barrier, ΔF the Helmholtz free energy, k the Boltzman constant, T the temperature in Kelvin (K), τ^i the resolved shear stress, τ_c^i the critical resolved shear stress, γ_0 the shear strain that is work conjugate to the resolved shear stress, ΔV the activation volume, l the pinning distance, and ψ is a coefficient that indicates that not all statistically stored dislocations (SSDs) necessarily act as pinning points. Note that each slip system becomes active when the resolved shear stress is equal or greater than the critical resolved shear stress ($\tau^i \geq \tau_c^i$). Further detail of the subsequent implicit integration of the constitutive equations and the determination of the consistent elastic-plastic tangent stiffness can be found in Dunne et al [10]. The crystal model is implemented within an ABAQUS user-defined subroutine (UMAT) which facilitates finite element modelling of single and bi-crystals in this study. The material properties used for the slip rule in the crystal plasticity model are given in Appendix B where the <*a*> and <*c*+*a*> type systems are differentiated (*a c/a* ratio of 1.593 is used), and the slip systems for an hcp single crystal are shown in Fig. 3(d). The critical resolved shear stresses for a representative near-alpha titanium alloy were taken from the experimental results of Gong and Wilkinson [31] and nominal strain γ_0 has been fixed for simplicity. Burger's vector magnitudes, frequency of dislocation jumps, and initial density of SSDs are obtained from standard property data and included in Appendix B. In some of the plasticity analyses carried out (which is made explicitly clear in the text), Mises perfect plasticity is assumed, and in this case a yield stress of 462 MPa is employed which corresponds to the critical resolved shear stress for single-crystal *a*-type slip.

3.1 Edge Crack Crystallographic Slip and its Crystal Orientation Dependence

We return to the edge crack problem in a homogeneous single crystal schematically shown in Fig. 6 but now allow for the development of plasticity in two ways. Firstly, the crystal plasticity model described above is employed which takes full account of the anisotropy of slip in hcp crystals and secondly, by employing standard isotropic Mises plasticity (while in both cases retaining the effects of elastic anisotropy). To begin, the x-direction stresses are determined using both approaches, and in the case of the crystal model, the hcp grain is orientated at φ=45°; that is, with its c-axis at 45° to the x-direction shown in Fig. 3(d). The results are shown in Fig. 11 in which near-identical stresses are developed.

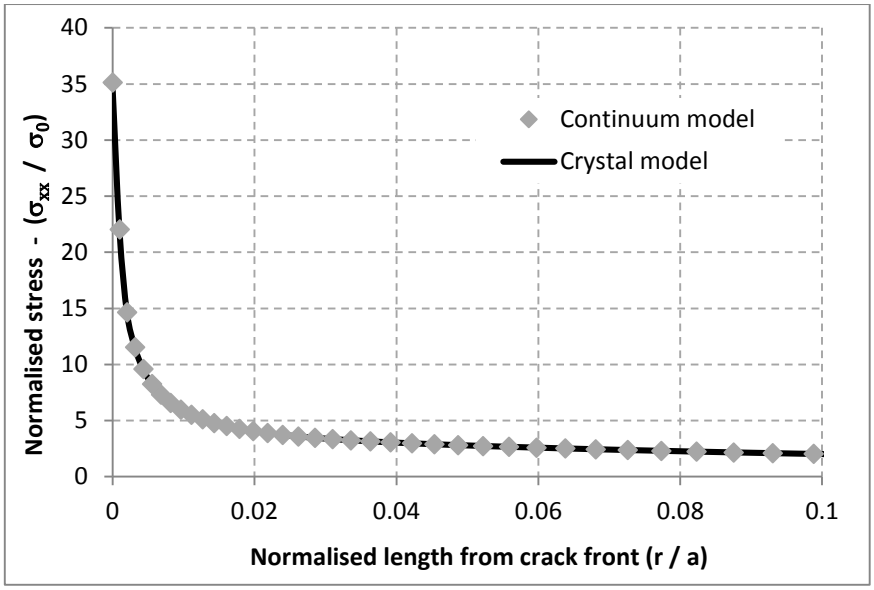

Figure 11 - Comparison of normalized σ_{xx} stresses obtained from crystal and Mises plasticity models along the x-direction from the crack tip.

The behaviour is explored further in Fig. 12 in which field variations of the y-direction stresses are shown for purely (anisotropic) elasticity, for crystal plasticity and for Mises plasticity, for the four crystallographic orientations (φ=0°, 45°, 60°, 90°) shown in the figure. The first (and expected) clear feature is the elimination of the highly localised stress concentration by incorporation of plasticity. The second is that the incorporation of anisotropic hcp crystal slip (as opposed to Mises plasticity) has limited effect on the resulting crack tip stress distributions, even as the crystallographic orientation is varied. Note that the width of the contour plots in Fig. 12 is 0.21 μm, so showing very local stresses.

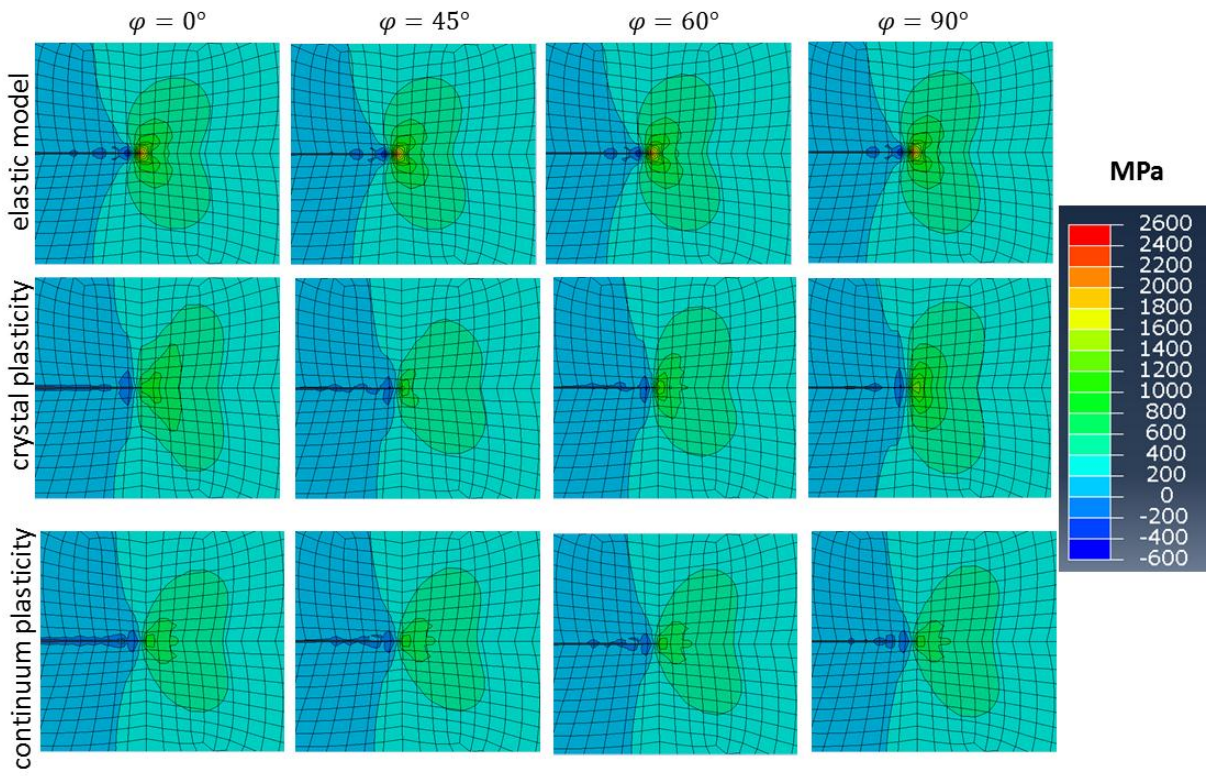

Figure 12 - Field variations of the direct stress component σ_{yy} around the crack tip for the single crystal model

In order to provide more detailed and quantitative assessments of the stresses determined using Mises elasto-plastic versus crystal plasticity, the normalized stress components (σ_{xx}/σ_0) and (σ_{yy}/σ_0) along the x-direction from the crack tip are extracted and shown for the crystallographic orientations (φ=0°, 45°, 60°, 90°) in Fig. 13 (a-b).

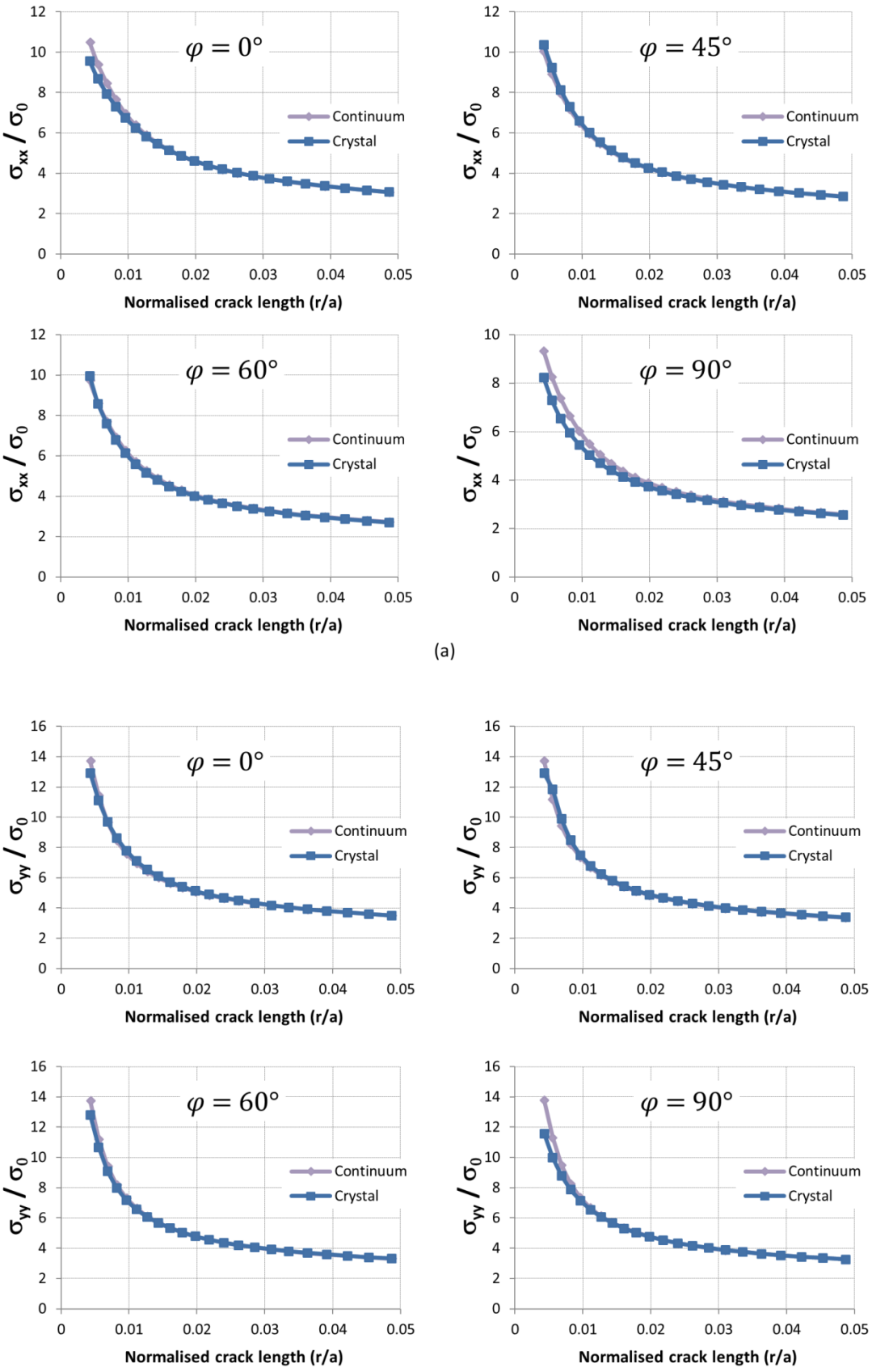

Figure 13 - Comparison between Mises and crystal plasticity models along the x-direction from the crack tip for the normalized stress components of (a) σ_{xx} and (b) σ_{yy}

Some differences in the stresses arise between the two models very close to the crack tip, but largely they are near-identical remote from the crack tip in the elastic zone. The small differences in the plastic region result from the hcp crystal anisotropy for which the differing strengths of the <a>-type and <c+a>-type slip are accounted. However, much more significant differences are anticipated in the plastic fields, and these are assessed next.

Fig. 14 shows the accumulated plastic strains calculated using the crystal and Mises plasticity models respectively for the crystallographic orientations (φ=0°, 45°, 60°, 90°) shown. Here, quite different distributions of plastic strain are observed resulting from the incorporation of crystal slip, and a strong dependence on crystal orientation exists which naturally the Mises model fails to capture. The crystal plasticity result for the particular asymmetric crystal orientation (φ= 60°) shows the development of a correspondingly asymmetric plastic strain field. It is also interesting to note the very different plastic fields developed for the two extreme crystal orientations of φ=0° and 90°. For the former, the slip is accommodated by a-type prismatic systems whereas in the latter, because of orientation, the slip occurs on the pyramidal slip systems with a significantly higher strength than that for the prismatics. As a result, the slip is much more localised and largely constrained to occur in a vertical band.

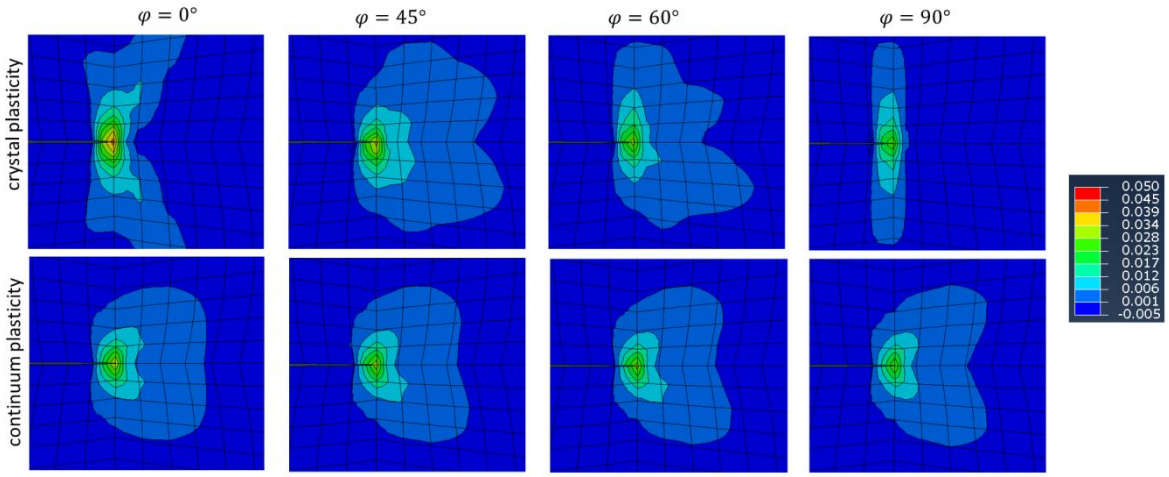

Figure 14 - Accumulated plastic strains obtained from the Mises and crystal plasticity models for the single crystal crystallographic orientations shown (0.1μm width plots).

Also, the highest values of the plastic strains are obtained for the reference crystal orientation (φ=0°) in which the grain is well-orientated for a-type slip. The magnitude of the accumulated plastic strain reduces with crystal orientation about the *x*-axis and takes the minimum value at φ=90°. In fact, the Mises plasticity results show a somewhat similar trend in plastic strain magnitude, but nothing like to the same extent. This follows from the effect

of the elastic anisotropy influencing stress state at the crack tip as a result of the crystal orientation.

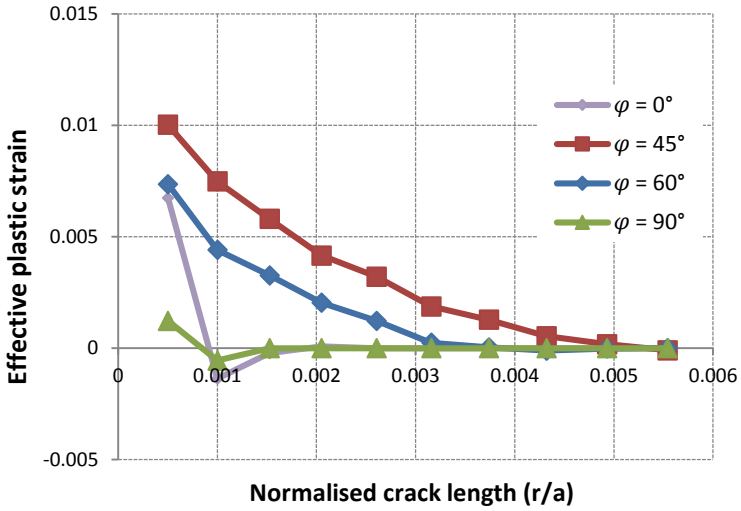

Figure 15 - Comparison of accumulated plastic strains along the x-direction from the crack front for the single crystal crystallographic orientations shown using the crystal plasticity model.

Fig. 15 shows the comparison of the effective plastic strains developed along the x-direction for the crystal orientations shown from the crystal plasticity model. Again it can be seen that the largest and smallest plastic strains at the crack front develop for the crystallographic orientations φ=0° and 90° respectively. While for these two cases, the accumulated plastic strains decay in a short distance from the crack front, the plastic strain field for φ=45° persists considerably further resulting from the favourable crystal orientation facilitating prismatic and basal slip. A comparison of the effective plastic strain distributions along the x-direction from the crack front resulting from crystal and Mises plasticity for the case of the reference crystal orientation (φ=0°) is shown in Fig. 16. Both models lead to similar trends of plastic strain but the crystal model demonstrates more localisation and the Mises model overestimates both the magnitude and extent of plasticity at the crack tip.

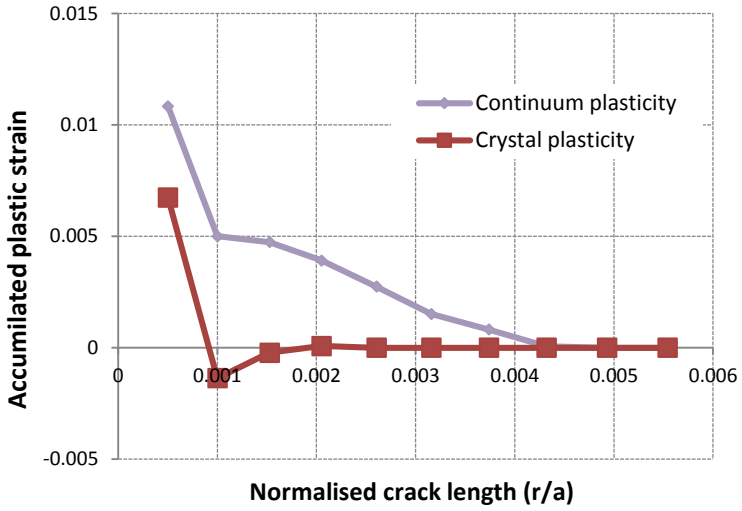

Figure 16 - Effective plastic strain distributions along the x-direction from the crack front for the crystal and Mises plasticity models for crystal orientation φ=0°

3.2 Edge Crack Crystallographic Slip in a Bi-crystal

Finally, we consider the bi-crystal shown schematically in Fig. 9 and investigate the effects of differing combinations of crystal orientations and the size of grain A relative to grain B using the crystal model. For this purpose, four different widths of the grain *A* were utilized (5, 7.5, 9 and 9.5 μm respectively). Firstly, the crystallographic orientations of grains *A* and *B* are selected to be φ=0° and 90° respectively and the results for this configuration are shown in Fig. 17(a). Secondly, Fig. 17(b) shows results for the configuration in which the crystallographic orientations of grains *A* and *B* are φ=90°and 0° respectively. Similar to results shown for stress intensity factors presented above, it can be seen that the accumulated plastic strains local to the crack tip are strongly affected by the crystallographic orientation combinations of two adjacent grains. Grain neighbours containing a crack can therefore have a significant effect on the plastic strain fields developed local to the crack tip.

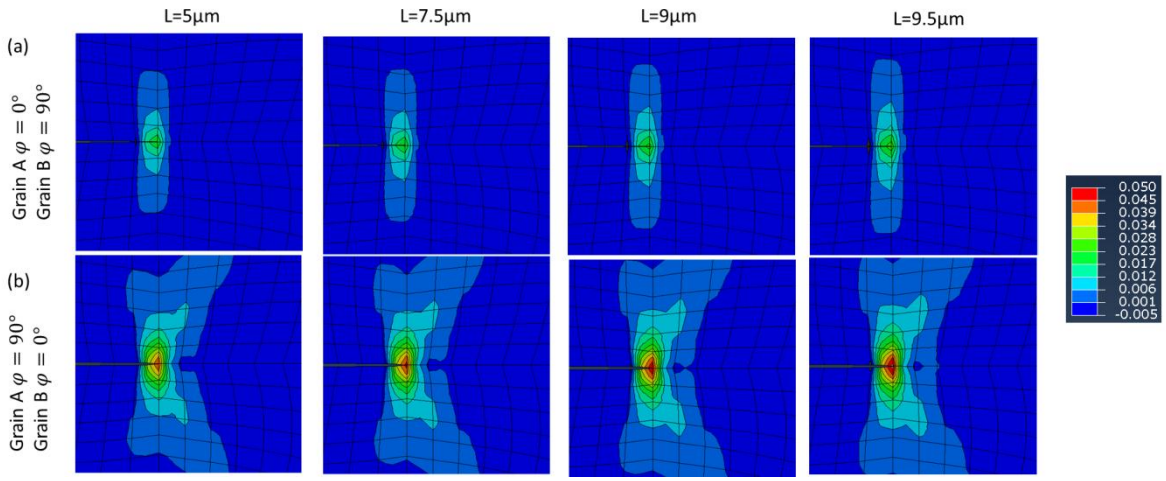

Figure 17 - Effect of the size of Grain *A* on the accumulated plastic strain local to the crack tip in Grain *B* for (a) Grain *A* φ=0°, Grain *B* φ=90° and (b) Grain *A* φ=90°, Grain *B* φ=0° (L = grain length, plot is 0.1□m in width)

4. Conclusions

An analytical solution for an edge crack in a representative hcp Ti single crystal subject to remote uniaxial stress shows that the stresses normal to the crack are independent of crystallographic orientation but small variations in the other stress components result. The stress intensity, however, remains independent of crystallographic orientation.

Studies of an edge crack in a bi-crystal show that the stress intensity depends on both the crystallographic orientation of the grain in which the crack tip terminates, and on the misorientation of the bi-crystal. The stresses local to an edge crack in a single crystal in which plasticity is allowed to develop show little dependence on crystallographic orientation such that the results obtained from both crystal and Mises plasticity are largely indistinguishable.

The plastic zone which develops at the tip of an edge crack in the hcp single crystal is strongly dependent on crystallographic orientation and is typically much more localised than that observed using Mises plasticity. Significant differences result in both the magnitude and extent of the plasticity at the crack tip with crystallographic orientation which can be quite different to that predicted using Mises plasticity. For an edge crack terminating in a bi-crystal, the slip fields which result depend upon the misorientation and grain morphology.

5. Acknowledgements

We are grateful to the Engineering and Physical Sciences Research Council (EP/G004676/1), and Rolls-Royce plc for financial support.

6. References

[1] M. Bache, 'A review of dwell sensitive fatigue in titanium alloys: the role of microstructure, texture and operating conditions', International Journal of Fatigue, vol. 25 (9–11), pp. 1079–1087, 2003.

[2] G. Lütjering and J. J. C. Williams, Titanium : Springer, 2007.

[3] R. R. Boyer, 'An overview on the use of titanium in the aerospace industry', Materials Science and Engineering: A, vol. 213 (1–2), pp. 103–114, 1996.

[4] S. Ghosh, M. Mills, S. Rokhlin, V. Sinha, W. O. Soboyejo, and J. C. Williams, 'The evaluation of cold dwell fatigue in Ti-6242', U.S. Dept. of Transportation / Federal Aviation Authority report, DOT/FAA/AR-06/24, 2007.

[5] M. Bache, M. Cope, H. Davies, W. Evans, and G. Harrison, 'Dwell sensitive fatigue in a near alpha titanium alloy at ambient temperature', International Journal of Fatigue, vol. 19 (93), pp. 83–88, 1997.

[6] D. Rugg, M. Dixon, and F. P. Dunne, 'Effective structural unit size in titanium alloys', The Journal of Strain Analysis for Engineering Design, vol. 42 (4), pp. 269–279, 2007.

[7] V. Hasija, S. Ghosh, M. J. Mills, and D. S. Joseph, 'Deformation and creep modeling in polycrystalline Ti–6Al alloys', Acta Materialia, vol. 51 (15), pp. 4533–4549, 2003.

[8] V. Sinha, M. J. Mills, and J. C. Williams, 'Understanding the contributions of normal-fatigue and static loading to the dwell fatigue in a near-alpha titanium alloy', Metallurgical and Materials Transactions A, vol. 35 (10), pp. 3141–3148, 2004.

[9] G. Venkataramani, D. Deka, S. Ghosh, and J. B. Nordholt, 'Crystal plasticity based FE model for understanding microstructural effects on creep and dwell fatigue in Ti-6242', ASME Journal of Engineering Materials and Technology, vol. 128 (3), pp. 356-365, 2006.

[10] F. P. E. Dunne, D. Rugg, and A. Walker, 'Lengthscale-dependent, elastically anisotropic, physically-based hcp crystal plasticity: Application to cold-dwell fatigue in Ti alloys', International Journal of Plasticity, vol. 23 (6), pp. 1061–1083, 2007.

[11] D. L. Davidson and D. Eylon, ‘Titanium alloy fatigue fracture facet investigation by selected area electron channeling’, Metallurgical Transactions A, vol. 11 (5), pp. 837–843, 1980.

[12] W. J. Evans and M. R. Bache, ‘Dwell-sensitive fatigue under biaxial loads in the near-alpha titanium alloy IMI685’, International Journal of Fatigue, vol. 16 (7), pp. 443–452, 1994.

[13] V. Sinha, J. E. Spowart, M. J. Mills, and J. C. Williams, ‘Observations on the faceted initiation site in the dwell-fatigue tested Ti-6242 alloy: Crystallographic orientation and size effects’, Metallurgical and Materials Transactions A, vol. 37 (5), pp. 1507–1518, 2006.

[14] J. R. Rice, “Tensile crack tip fields in elastic-ideally plastic crystals,” Mech. Mater., vol. 6, no. 4, pp. 317–335, Dec. 1987.

[15] J. R. Rice and M. Saeedvafa, “Crack tip singular fields in ductile crystals with taylor power-law hardening. I: Anti-plane shear,” J. Mech. Phys. Solids, vol. 36, no. 2, pp. 189–214, 1988.

[16] M. Saeedvafa and J. R. Rice, “Crack tip singular fields in ductile crystals with taylor power-law hardening: II: Plane strain,” J. Mech. Phys. Solids, vol. 37, no. 6, pp. 673–691, 1989.

[17] J. R. Rice, D. E. Hawk, and R. J. Asaro, “Crack tip fields in ductile crystals,” in Non-Linear Fracture, W. G. Knauss and A. J. Rosakis, Eds. Springer Netherlands, 1990, pp. 301–321.

[18] V. Gupta, “Tensile crack-tip fields in elastic-ideally plastic hexagonal crystals and layered materials,” Acta Met. Mater., vol. 41, no. 11, pp. 3223–3236, Nov. 1993.

[19] A. M. Cuitiño and M. Ortiz, “Three-dimensional crack-tip fields in four-point-bending copper single-crystal specimens,” J. Mech. Phys. Solids, vol. 44, no. 6, pp. 863–904, Jun. 1996.

[20] Stroh, AN, ‘The formation of cracks as a result of plastic flow’, Proceedings of Royal Society A, vol. 223, pp. 404-414, 1954.

[21] K. Kirane and S. Ghosh, ‘A cold dwell fatigue crack nucleation criterion for olycrystalline Ti-6242 using grain-level crystal plasticity FE model’, International Journal of Fatigue, vol. 30, pp. 2127-2139, 2008.

[22] F.P.E. Dunne and D. Rugg, ‘On the mechanisms of fatigue facet nucleation in titanium alloys’, Fatigue & Fracture of Engineering Materials & Structures, vol. 31, pp. 949-958, 2008.

[23] S.G. Lekhnitskii, Theory of Elasticity of an Anisotropic Body, First English Language. Mir, 1981.

[24] H. Liebowitz, Fracture, an advanced treatise. Academic Press, 1968.

[25] G.C. Sih, P.C. Paris, and G.R. Irwin, 'On cracks in rectilinearly anisotropic bodies', International Journal Fracture, vol. 1 (3), pp. 189–203, 1965.

[26] D.E. Lempidaki, N.P. O'Dowd, and E.P. Busso, 'Crack Tip Stress Fields for Anisotropic Materials with Cubic Symmetry', 15th European Conference of Fracture, Stockholm, Sweden, 2004.

[27] H. J. Bunge, *Texture analysis in materials science: mathematical methods*. Butterworths, 1982.

[28] G. Bao, S. Ho, Z. Suo, and B. Fan, "The role of material orthotropy in fracture specimens for composites," Int. J. Solids Struct., vol. 29, no. 9, pp. 1105–1116, 1992.

[29] W. F. Brown and J. E. Srawley, 'Plane Strain Crack Toughness Testing of High Strength Metallic Materials'. American Society for Testing and Materials, 1966.

[30] J.R. Rice, 'A path independent integral and the approximate analysis of strain concentration by notches and cracks', Journal of Applied Mechanics, vol. 35, pp. 379-386, 1968.

[31] J. Gong and A.J. Wilkinson, 'Anisotropy in the plastic flow properties of single-crystal alpha titanium determined from micro-cantilever beams', Acta Materialia, vol. 57 (19), pp. 5693-5705, 2009.

APPENDIX A – 3D Rotations

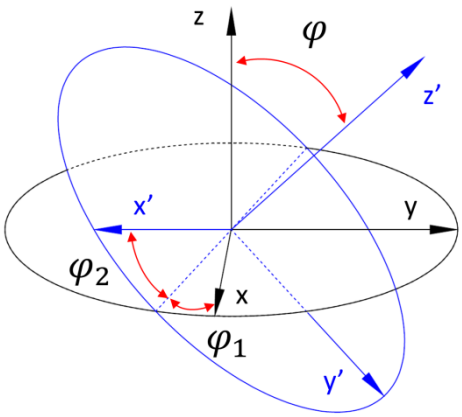

$$\boldsymbol{R}_{\varphi_1} = \begin{bmatrix} \cos\varphi_1 & \sin\varphi_1 & 0 \\ -\sin\varphi_1 & \cos\varphi_1 & 0 \\ 0 & 0 & 1 \end{bmatrix}; \; \boldsymbol{R}_{\varphi} = \begin{bmatrix} 1 & 0 & 0 \\ 0 & \cos\varphi & \sin\varphi \\ 0 & -\sin\varphi & \cos\varphi \end{bmatrix}; \quad \boldsymbol{R}_{\varphi_2} = \begin{bmatrix} \cos\varphi_2 & \sin\varphi_2 & 0 \\ -\sin\varphi_2 & \cos\varphi_2 & 0 \\ 0 & 0 & 1 \end{bmatrix}$$

Combining all three rotations:

$$\boldsymbol{R} = \boldsymbol{R}_{\varphi_1}\boldsymbol{R}_{\varphi}\boldsymbol{R}_{\varphi_2} \qquad \text{A.1}$$

such that the full rotation matrix is:

$$\boldsymbol{R} = \begin{bmatrix} \cos\varphi_1\cos\varphi_2 - \sin\varphi_1\sin\varphi_2\cos\varphi & \sin\varphi_1\cos\varphi_2 + \cos\varphi_1\sin\varphi_2\cos\varphi & \sin\varphi_2\sin\varphi \\ -\cos\varphi_1\sin\varphi_2 - \sin\varphi_1\cos\varphi_2\cos\varphi & -\sin\varphi_1\sin\varphi_2 + \cos\varphi_1\cos\varphi_2\cos\varphi & \cos\varphi_2\sin\varphi \\ \sin\varphi_1\sin\varphi & -\cos\varphi_1\sin\varphi & \cos\varphi \end{bmatrix}$$

(In future entries from this matrix will be abbreviated as R_{11}, R_{12} etc.)

And as before define stress rotations as:

$$\boldsymbol{\sigma}' = \boldsymbol{R}\ \boldsymbol{\sigma}\ \boldsymbol{R}^T$$

Such that:

$$\underline{\sigma}' = \begin{bmatrix} R_{11} & R_{12} & R_{13} \\ R_{21} & R_{22} & R_{23} \\ R_{31} & R_{32} & R_{33} \end{bmatrix} \begin{bmatrix} \sigma_{xx} & \sigma_{xy} & \sigma_{xz} \\ \sigma_{yx} & \sigma_{yy} & \sigma_{yz} \\ \sigma_{zx} & \sigma_{zy} & \sigma_{zz} \end{bmatrix} \begin{bmatrix} R_{11} & R_{21} & R_{31} \\ R_{12} & R_{22} & R_{32} \\ R_{13} & R_{23} & R_{33} \end{bmatrix} \quad \text{A.2}$$

Gathering the rotation terms and converting the stress tensors to vectors:

$$\underline{\sigma}' = \boldsymbol{T}\,\underline{\sigma} \quad \text{A.3}$$

where:

$$\boldsymbol{T} = \begin{bmatrix} R_{11}^2 & R_{12}^2 & R_{13}^2 & 2R_{12}R_{13} & 2R_{11}R_{13} & 2R_{11}R_{12} \\ R_{21}^2 & R_{22}^2 & R_{23}^2 & 2R_{22}R_{23} & 2R_{21}R_{23} & 2R_{21}R_{22} \\ R_{31}^2 & R_{32}^2 & R_{33}^2 & 2R_{32}R_{33} & 2R_{31}R_{33} & 2R_{31}R_{32} \\ R_{21}R_{31} & R_{22}R_{32} & R_{23}R_{33} & R_{23}R_{32}+R_{22}R_{33} & R_{23}R_{31}+R_{21}R_{33} & R_{22}R_{31}+R_{21}R_{32} \\ R_{11}R_{31} & R_{12}R_{32} & R_{13}R_{33} & R_{13}R_{32}+R_{12}R_{33} & R_{13}R_{31}+R_{11}R_{33} & R_{12}R_{31}+R_{11}R_{32} \\ R_{11}R_{21} & R_{12}R_{22} & R_{13}R_{23} & R_{13}R_{22}+R_{12}R_{23} & R_{13}R_{21}+R_{11}R_{23} & R_{12}R_{21}+R_{11}R_{22} \end{bmatrix}$$

$$[\boldsymbol{S}]_{3D\ Rot} = [\boldsymbol{T}]^T[\boldsymbol{S}][\boldsymbol{T}] \quad \text{A.4}$$

This is the matrix used to calculate the rotated compliance matrix, its derivation may be found in standard mechanics texts.

APPENDIX B – Material Properties

Elastic stiffness matrix

$$C = \begin{pmatrix} 162530 & 92000 & 70000 & 0 & 0 & 0 \\ 92000 & 162530 & 70000 & 0 & 0 & 0 \\ 70000 & 70000 & 181660 & 0 & 0 & 0 \\ 0 & 0 & 0 & 35270 & 0 & 0 \\ 0 & 0 & 0 & 0 & 46700 & 0 \\ 0 & 0 & 0 & 0 & 0 & 46700 \end{pmatrix} \text{MPa}$$

Slip rule material properties

	τ_c (MPa)	b (μm)	k (JK^{-1})	ΔF (J)	ν (s^{-1})	$\rho_s^m = \rho_s^s$ (μm^{-2})	γ_0	ψ
<a> slip	200	3.2×10^{-4}	1.38×10^{-23}	3.456×10^{-20}	10^{11}	0.05	8.33×10^{-6}	1.5×10^{-4}
<c+a> slip	500	5.1×10^{-4}						